Journal Pre-proof

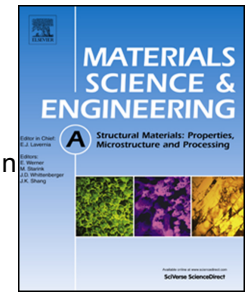

Phase evolution and mechanical properties of an intercritically-annealed Fe-10Ni-7Mn (wt. %) martensitic steel severely deformed by high-pressure torsion

Faezeh Javadzadeh Kalahroudi, Hamidreza Koohdar, Terence G. Langdon, Mahmoud Nili-Ahmadabadi

PII: S0921-5093(20)31582-3

DOI: https://doi.org/10.1016/j.msea.2020.140519

Reference: MSA 140519

To appear in: *Materials Science & Engineering A*

Received Date: 30 June 2020

Revised Date: 21 October 2020

Accepted Date: 9 November 2020

Please cite this article as: F.J. Kalahroudi, H. Koohdar, T.G. Langdon, M. Nili-Ahmadabadi, Phase evolution and mechanical properties of an intercritically-annealed Fe-10Ni-7Mn (wt. %) martensitic steel severely deformed by high-pressure torsion *Materials Science & Engineering A*, https://doi.org/10.1016/j.msea.2020.140519.

CRediT author statement

Faezeh Javadzadeh Kalahroudi: Conceptualization, Validation, Investigation, Resources, Writing - Original Draft, Writing - Review & Editing, Visualization

Hamidreza Koohdar: Conceptualization, Validation, Resources, Writing - Review & Editing

Terence G. Langdon: Resources, Writing - Review & Editing

Mahmoud Nili-Ahmadabadi: Conceptualization, Validation, Resources, Writing - Review & Editing, Supervision, Project administration, Funding acquisition

Phase evolution and mechanical properties of an intercritically-annealed Fe-10Ni-7Mn (wt. %) martensitic steel severely deformed by high-pressure torsion

Faezeh Javadzadeh Kalahroudi [a], Hamidreza Koohdar [b], Terence G. Langdon [c], Mahmoud Nili-Ahmadabadi [a, d, *]

[a] *School of Metallurgy and Materials Engineering, University of Tehran, P.O. Box 14395-731, Tehran, Iran*

[b] *School of Metallurgy and Materials Engineering, Iran University of Science and Technology, Tehran, Iran*

[c] *Materials Research Group, Department of Mechanical Engineering, University of Southampton, Southampton SO17 1BJ, UK*

[d] *Center of Excellence for High Performance Materials, School of Metallurgy and Materials Engineering, University of Tehran, Tehran, Iran*

Abstract

Experiments were conducted on an Fe-10Ni-7Mn (wt. %) martensitic steel processed by high-pressure torsion (HPT) after intercritical annealing in the dual phase (α+γ) region at 600˚C for 2 hours. Microstructural examination and phase analysis using electron backscatter diffraction (EBSD) confirmed that post-HPT processing led to a phase transformation of austenite to α′-martensite (γ→α′ and γ→ε→α′) such that after 20 turns of HPT the microstructure included multi-phases of α′-martensite, austenite and ε-martensite. The HPT processing also produced a significant reduction in the α′-martensite and austenite grain sizes from initial values of ~3.8 and ~3.9 μm to ~225 and ~60 nm after 20 HPT turns, respectively, while the ε-martensite final grain size was ~44 nm. Micro-hardness measurements and tensile testing showed a significant increase in hardness and in the ultimate tensile strength to about 680 Hv and 2235 MPa after 20 turns, respectively. Finally, the fracture surfaces of samples after HPT processing showed a combination of dimples, cracks and shear bands which confirmed a transition in fracture behavior from ductile to a mixture of a ductile and brittle mode.

Keywords: High-pressure torsion; Intercritical annealing; Phase transformation; Microstructural evolution; Mechanical properties

* Corresponding author
E-mail address: *nili@ut.ac.ir (M. Nili-Ahmadabadi)*
Tel.: 098-2182084078

1. Introduction

Processing by severe plastic deformation (SPD) refers to metal forming procedures in which very high strains are applied to samples to introduce significant grain refinement. These procedures are typically applied at low temperatures without introducing any significant changes in the overall dimensions of the processed sample [1]. High-pressure torsion (HPT) is an SPD method in which a disk-shaped sample is subjected to torsional shear straining under an extreme hydrostatic pressure [2]. A key advantage of this process is that it produces samples having exceptionally high shear strains [3]. The equivalent strain can be calculated by using the expression:

$$\varepsilon_{eq} = \frac{2\pi Nr}{\sqrt{3}t} \quad (1)$$

where N, r and t are the number of turns of HPT processing, the distance from the center of the sample and the thickness of the sample, respectively. According to Eq. (1), during HPT processing a strain gradient is produced along the diameter of the disk with the smallest strain in the center and the highest strain at the outer edge of the sample [4].

Processing by HPT has become attractive over the last two decades due to the ability to produce a range of improved properties including grain refinement even to the nanometer scale [5, 6], high densities of lattice defects such as vacancies, dislocations and free volume-type defects [7-9], high strength and hardness [10], reasonable thermal stability [11, 12], superplastic elongations [13, 14], shape memory effects [15], improved hydrogen embrittlement resistance [16], induced phase transformations [17-20] and supersaturated solid solutions [21, 22]. In addition, by comparison with other SPD techniques such as equal-channel angular pressing (ECAP) [23], processing by HPT produces a higher fraction of grain boundaries having high angles of misorientation [24].

The Fe-10Ni-7Mn (wt. %) alloy is a representative high strength low carbon steel having a fully lath martensitic microstructure in the solution annealed (SA) condition. This steel may be age-hardened by the formation of nanometer-sized intermetallic precipitates such as f.c.t θ-NiMn, but it suffers from intergranular embrittlement due to a discontinuous coarsening of the grain boundary precipitates [25]. Recent studies have focused on applying various SPD processes to this steel in order to improve its mechanical properties. Thus, the effects of ECAP [26], severe cold rolling [27-29], repetitive corrugation and straightening by rolling (RCSR) [30] and HPT [31] have been investigated. Several studies have examined intercritical annealing of this martensitic steel in the dual phase (α+γ) region at temperatures between 570 and 630˚C and focused on the reversed austenite formation and related mechanisms. It appears that when the heating rate is 20 ˚C/s and the annealing temperature is below 585˚C, a reverse transformation of martensite to austenite occurs through a mixed diffusion-controlled mechanism due to a combination of bulk diffusion and diffusion along the interface. However, if the temperature is above 585˚C, a reverse transformation takes place through a sequential combination of both non-diffusional and diffusional mechanisms [32]. It was also reported that intercritical annealing at 600 ˚C for 2 hours gave the highest amount of retained austenite in the microstructure [33] whereas longer holding times led to the growth of higher volume fractions of non-diffusional austenite grains which ultimately transformed to martensite during cooling and thereby reduced the amount of retained austenite.

The present steel with a martensitic microstructure was recently subjected to HPT processing and the subsequent microstructure, mechanical properties and thermal features were investigated [31]. However, the effect of intercritical annealing, which transforms the single phase of martensite to the dual phases of austenite and martensite, has not been studied in

samples subjected to HPT processing although it is reasonable to anticipate that the combination of intercritical annealing and HPT processing may lead to the microstructural evolution of the refined grains and this will have a significant impact on the mechanical properties of the alloy. Accordingly, the present study was initiated in order to examine the effect of combining an intercritical annealing at 600˚C for 2 hours with post-HPT processing through different numbers of turns at room temperature. The overall objective was to provide a comprehensive overview of the microstructures, phase evolution and mechanical properties of the processed samples.

2. Material and experimental methods

The chemical composition of the Fe-10Ni-7Mn (wt. %) martensitic steel is given in Table 1. Samples were prepared using a vacuum induction melting (VIM) furnace and a vacuum arc remelting (VAR) furnace. Then hot forging was performed at 1150 ˚C for 50% following by homogenization in a vacuum furnace at 1200 ˚C for 24 hours. Afterwards, the ingot was solution annealed at 950 ˚C for 1 hour and ultimately the samples were quenched in cold water to obtain a fully martensitic microstructure.

Table 1. Chemical composition of the investigated steel.

Element	Fe	Ni	Mn	C	S	P	N	Al
wt. %	Bal.	10.05	6.97	0.005	0.006	0.005	0.005	0.003

All samples were intercritically annealed (IA) in a neutralized salt bath in the dual phase ($\alpha+\gamma$) region at 600 °C for 2 hours since this holding time leads to the largest amount of austenite phase in the microstructure [33] and then they were quenched in cold water in order to form a dual phase microstructure of α'-martensite and austenite. Samples were prepared with 2 mm thickness so that a required heating rate of 20 ˚C/s was achieved to give austenite formation as reported previously [32]. In order to apply HPT processing, disk-shape samples were cut with

diameters of 10 mm and thicknesses of 0.8 mm. All disks were processed by HPT at room temperature with an applied pressure of 6.0 GPa and a rotation rate of 1 rpm for 1, 3, 6, 10 or 20 turns under quasi-constrained conditions [34].

Field emission scanning electron microscopy (FESEM) using an electron backscatter diffraction (EBSD) detector was used for microstructural and phase analysis. Samples were mechanically polished and then electrolytically etched in a 900 ml CH3COOH + 100 ml HClO4 solution at approximately 11 °C with a voltage of 20 V. The EBSD images were taken with a step size of 0.2 μm and evaluated using TSL-orientation imaging microscopy (OIM) analysis software. The observation region is shown in the schematic illustration in Fig. 1.

The Vickers micro-hardness was measured with a load of 100 gf and dwell times of 10 s across the diameters of the disks at separations of 1 mm as shown in Fig. 1. Tensile test samples were cut from off-center positions at a distance of 2.5 mm from the centers of the disks with gauge lengths of 1.8 mm, widths of 0.8 mm and thicknesses of 0.5 mm. The tensile tests were performed using a SANTAM tensile testing machine at room temperature with initial strain rates of 5.0×10^{-4} s^{-1}. Additionally, the fracture surfaces of tensile test samples were examined using a scanning electron microscope (SEM).

3. Experimental results

3.1. Microstructure and phase evolution

Fig. 2 displays grain boundary images superimposed on EBSD phase maps for (a) the SA sample, (b) the IA sample at 600 °C and (c-e) HPT-processed samples after 1, 6 and 20 turns in which the pink, green and yellow colors denote the α′-martensite, austenite and ε-martensite phases, respectively. The superimposed black and red lines correspond to high-angle grain

boundaries (HAGBs) and low-angle grain boundaries (LAGBs), respectively. The EBSD images show that the SA sample is fully lath martensitic with a large fraction of LAGBs whereas intercritical annealing at 600 ˚C leads to a dual phase microstructure of austenite and α′-martensite with grain sizes of about 3.9 and 3.8 μm, respectively.

After one turn of HPT processing in Fig. 2(c) there is an elongated microstructure along the shear direction including a mixture of the α′-martensite, austenite and ε-martensite phases. By increasing the HPT straining, the microstructure evolves to a combination of equiaxed and elongated grains and ultimately, after 6 turns in Fig. 2(d), forms a fully equiaxed and homogenous microstructure. The volume fractions of austenite and ε-martensite decrease drastically by further straining and after 20 turns in Fig. 2(e) the microstructure is nearly fully α′-martensitic with very few nano-grains of austenite and ε-martensite. The average grain size values were measured using the linear intercept method which is shown in Table 2.

Table 2. Average grain sizes of the different phases obtained from EBSD images.

	α′-martensite	austenite	ε-martensite
SA	□ 5.5 μm	-	-
IA at 600°C	□ 3.8 μm	□ 3.9 μm	-
IA at 600°C + HPT (N=1)	□ 546 nm	□ 385 nm	□ 435 nm
IA at 600°C + HPT (N=6)	□ 524 nm	□ 107 nm	□ 221 nm
IA at 600°C + HPT (N=20)	□ 223 nm	□ 62 nm	□ 44 nm

The volume fractions of the different phases obtained from the EBSD data are presented in Fig. 3 for various experimental conditions. It is clear that the Fe-10Ni-7Mn (wt. %) alloy has a fully martensitic microstructure in the SA condition but after intercritical annealing at 600˚C for 2 hours the microstructure consists of austenite and α′-martensite phases with volume fractions of ~48 and ~52%, respectively. A phase analysis of the 1-turn HPT sample shows austenite, α′-

martensite and about 31% of ε-martensite but gradually, by increasing the numbers of turns, the amounts of austenite and ε-martensite decrease and finally the microstructure has more than 90% of α′-martensite after 20 turns.

3.2. Mechanical properties

Fig. 4(a) shows the micro-hardness distributions of the IA and HPT-processed samples for different numbers of turns with the center of the disk located at the ordinate: the lower dashed line at ~288 Hv denotes the measured micro-hardness in the IA sample. The hardness values after 1 turn of HPT processing display a sharp increase in hardness with values up to ~580 Hv at the periphery and ~400 Hv in the central region. By further straining, the measured values increase both in the center and the periphery and ultimately reach a maximum value of about 680 Hv at the edge. The hardness distribution tends towards, but does not fully attain, homogeneity across the disk diameter after 20 turns of HPT processing. The distribution of micro-hardness values as a function of equivalent strain is shown in Fig. 4(b). These results show an initial increase at low equivalent strains but a reasonable saturation in hardness at equivalent strains above about 110.

The engineering stress-strain curves are shown in Fig. 5 for samples in the SA condition, in the IA condition at 600˚C and after HPT-processing through 3, 10 and 20 turns. The measured values of the ultimate tensile strength (UTS), yield strength (YS) and fracture strain for different samples are summarized in Table 3 together with values reported earlier for the SA sample after HPT processing through the same numbers of turns [31]. In the SA sample the values of the UTS and fracture strain were ~830 MPa and ~16.5%, respectively, but after IA at 600˚C for 2 hours, the UTS was reduced to ~795 MPa and the fracture strain increased to ~27.8%. Finally, after 20

turns the UTS and elongation values reached ~2235 MPa and ~2.4%, respectively. These values are reasonably similar to the SA sample HPT-processed through 20 turns where the UTS and elongation were ~2230 MPa and ~3.1%, respectively [31].

Table 3. Values of ultimate tensile strength, yield strength and fracture strain for the samples.

	UTS (MPa)	YS (MPa)	Fracture Strain (%)	Ref.
SA	830	790	16.5	[31]
IA at 600°C	795	510	27.8	Present
IA at 600°C+ HPT (N=3)	1055	1040	20.3	Present
IA at 600°C+ HPT (N=10)	1600	1440	7.3	Present
IA at 600°C+ HPT (N=20)	2235	2150	2.4	Present
SA+ HPT (N=3)	1840	1800	10.2	[31]
SA+ HPT (N=10)	2115	1995	6.4	[31]
SA+ HPT (N=20)	2230	2040	3.1	[31]

The fracture surfaces of samples after tensile testing in the SA and IA conditions are shown at different magnifications in Fig. 6 (a, b) and (c, d), respectively. Additionally, SEM images of the fracture surfaces after 20 turns of HPT processing are given in Fig. 7. It is readily apparent that there are significant differences in the fracture morphologies of samples before and after HPT processing. In the SA (Fig. 6(a, b)) and IA samples (Fig. 6(c, d)), the surfaces show well-defined dimples with different sizes and depths which confirm the occurrence of a ductile facture mode. After HPT processing (Fig. 7), SEM images show combinations of ultrafine dimples and cracks and with shear bands in the fracture surfaces which demonstrate that the application of HPT processing leads to a transition in fracture behavior from ductile to a mixture of a ductile and brittle mode.

4. Discussion

4.1. Microstructure and phase evolution

It is concluded from the EBSD images in Fig. 2 and the data summarized in Fig. 3 that the austenite phase appears after intercritical annealing at 600˚C for 2 hours. Reports confirm that during continuous heating and isothermal annealing at 600˚C with a heating rate of 20˚C/s the austenite is reversed from the martensite by a sequential combination of two mechanisms including both diffusionless and diffusional mechanisms [32, 35]. The transition temperature from the diffusional to non-diffusional transformation was measured as close to 585˚C.

During processing by SPD, the retained austenite phase can transform to the α′-martensite directly (γ→ α′) and/or indirectly with the sequence of γ→ ε→ α′ [5, 18, 36]. Thus, processing by HPT can provide the necessary driving force for both of the above phase transformations in the present steel. Phase analysis results show that after one turn of HPT, a part of the austenite phase (~4%) transforms directly to α′-martensite and the other part, corresponding to ~31%, forms ε-martensite.

The development of ε-martensite with a hexagonal close-packed (hcp) structure as an intermediate phase is explained due to the low stacking-fault energy (SFE) of the present alloy [29]. Thus, ε-martensite can form on every second {111} plane of the fcc lattice and hence the ABCABC sequence in the fcc planes transforms into an hcp sequence of ABABAB. As a result of this transformation, the gliding of Shockley partial dislocations may lead to the appearance of ε-martensite under deformation [36, 37]. Based on earlier reports [33, 38], the SFE of the present steel is calculated as about 10 mJ/m^2. Since an SFE below 12 mJ/m^2 is required for the austenite to ε-martensite transformation by deformation, this alloy is accordingly susceptible to exhibiting this phase transformation during straining [38]. As the SFE becomes even lower, the formation of stacking faults becomes easier and hence the formation of an hcp structure from the fcc-austenite phase is further facilitated. Based on a report of the application of HPT processing to a

high manganese austenitic steel, the ε-martensite can be transformed from an austenite phase even under hydrostatic compression without any torsional strain and its volume fraction thereby increases in the early stages by adding a torsional strain [18].

The ε-martensite eventually transforms to α′-martensite at higher strains by a mechanism in which the α′-martensite forms within the ε-martensite plates. The α′-martensite embryos can nucleate at microscopic shear band (faults, twins and ε-martensite) intersections [39]. Since the number of these intersections increases with applied strain, the volume fraction of α′-martensite reaches a maximum value by further straining [40]. A similar trend in phase transformations during HPT processing was observed in a 316L austenitic stainless steel in which a totally austenitic microstructure transformed gradually to ε-martensite and α′-martensite, and eventually after 20 turns the main phase became α′-martensite [36].

In this research, the EBSD images reveal that during intercritical annealing the high density of LAGBs, which were present in the initial lath martensitic steel (Fig. 2(a)), declines sharply because of the reduction in the amount of α′-martensite and its annealing (Fig. 2(b)) [33]. After the first turn of HPT processing (Fig. 2(c)), the fraction of these boundaries increases again and in the next turns they transform into HAGBs. In the 20-turn HPT-processed sample (Fig. 2(e)), a high fraction of HAGBs is observed which is one of the important characteristics of HPT processing [41].

Table 2 demonstrates the capability of HPT processing in producing very significant grain refinement that is consistent with many earlier reports [10, 31]. As anticipated, HPT processing has a great effect on grain size and produces a reduction from ~3.8 μm to ~223 nm in the α′-martensite phase and ~3.9 μm to ~ 62 nm in the austenite phase after 20 turns. In addition, the grain size of the ε-martensite phase was measured as ~44 nm after 20 turns. The high density

of dislocations together with the phase transformations occurring during HPT processing ($\gamma \rightarrow \varepsilon$, $\varepsilon \rightarrow \alpha'$ and $\gamma \rightarrow \alpha'$) may contribute to these very significant reductions in grain sizes.

4.2. Mechanical properties

It follows from Fig. 4(a) that the observed difference in the measured micro-hardness values in the center and periphery regions of the samples is due to the high concentration of dislocations and the associated grain refinement caused by the higher imposed strain in the outer region. This micro-hardness distribution is consistent with the predictions of Eq. (1) and it is similar to results reported for many other materials processed by HPT [42, 43]. Thus, the observed difference decreases by increasing the imposed strain and, as is apparent in Fig. 4(a), after 20 turns a homogeneity is almost reached and the samples have two reasonably separate homogenous regions in the central and outer parts of the disks. The ability for achieving excellent homogeneity throughout HPT samples after high torsional straining is well established for other materials such as high-purity Al [44] and selective laser melted 316L stainless steel [45].

The nearly equal measured hardness values in the 6 and 10-turn HPT-processed samples (Fig. 4(a)) may indicate that applying HPT processing for these turns leads to similar structural features such as the density of dislocations and grain refinement in these samples. This may be a reasonable assumption since the reported values for the grain sizes after 6 and 20 turns of HPT processing (Table 2) are not significantly different. However, the hardness distribution with equivalent strain (Fig. 4(b)) shows a saturation in hardness which implies that the yielded structure reaches an almost saturated level so that achieving greater grain refinement by further straining may be difficult. Moreover, at the center of the samples there is theoretically no imposed strain based on Eq. (1) but the measured hardness is not zero and even increases by

increasing the numbers of turns. This is consistent with the behavior anticipated in the centers of HPT samples based on strain gradient plasticity modelling [46]. It is also possible that there was some small misalignment between the upper and lower anvils during the HPT processing and this may produce an additional shear strain in the central region of the samples and cause strain hardening [47-51].

After solution annealing, due to the high density of dislocations in the lath α′-martensite microstructure (Fig. 2(a)), there was insignificant strain hardening but, due to the ductile nature of the matrix, there was an earlier report of about 15% non-uniform elongation [31]. It appears that intercritical annealing causes an improvement in the total ductility and this is evidently due to the higher amount of austenite phase in the microstructure (Fig. 2(b)). In the 3-turn HPT-processed sample an increase in UTS and YS with a reduction in ductility is achieved but it is noteworthy that the sample has a higher elongation by comparison with the SA condition. This is explained by the multiphase microstructure including ductile austenite which is visible in the EBSD images (Fig. 2(c, d)) in the 1 and 6-turn HPT-processed samples. Since the austenite phase is observed in the microstructure of the samples after 1 and 6 turns, it is reasonable to expect that the 3-turns HPT sample also obeys this trend and has at least a few percent of austenite. Therefore, the combination of intercritical annealing and HPT processing after 3 turns produces a special microstructure with grain refinement that consequently leads to a suitable mixture of strength and ductility. By increasing the numbers of turns, different factors such as the ultrafine grains, higher density of dislocations and the presence of shear bands, together with the multiphase microstructure, lead to an enhancement in the UTS and YS and a reduction in ductility [36].

It is interesting to note that after 20 turns of HPT processing about a 130% enhancement in hardness values occurs whereas the tensile tests show about a 320% increase in yield strength. This non-proportional trend is in agreement with some reports on steels after HPT processing [5, 10, 51]. It was suggested that conversion of a macroscopically isotropic into an anisotropic nanostructure may cause this non-proportional evolution of hardness and yield strength during the HPT processing. Also, it was explained that in hardness measurements the complex stress state under the Vickers indenter implies a complex averaging over all orientations, whereas tensile strength is measured in the strongest direction [10]. Although these explanations rationalize, at least to some extent, the differences between the hardness and tensile strength increments after HPT processing, it seems that more studies are required.

Tensile tests reported earlier are also displayed as the three bottom rows of Table 3. It is important to note that the IA samples processed by HPT show lower ultimate and yield strengths and higher ductility by comparison with the SA HPT samples for low numbers of HPT through 3 and 10 turns. The lower values for the IA samples are attributed to the phase transformations and the presence of austenite and ε-martensite in the microstructure. In practice, different crystal structures will have different responses with respect to grain boundary strengthening effects and it was reported that grain boundaries in bcc materials hinder slip dislocations more efficiently than in fcc and hcp materials [41]. Thus, after 20 turns the microstructure is so distorted and includes less than 10% of austenite and ε-martensite phases (Fig. 2(e) and Fig. 3) so that the values of the UTS, YS and ductility in the IA and SA samples after HPT processing are reasonably similar (Table 3). This confirms the effect of the multiphase microstructure in softening of this alloy.

The SEM images of the fracture surfaces (Fig. 6 and 7) support the tensile tests results. The ductile surface of the IA sample (Fig. 6(c, d)) is consistent with the recorded ductility of about 28%. In addition, the fracture surface of the IA sample (Fig. 6(c, d)) shows larger dimples by comparison with the SA sample (Fig. 6(a, b)) and this gives a higher elongation. After applying HPT processing as reported elsewhere [31, 52], there is a transition in the fracture mode from necking to shearing and the fracture surfaces indicate a combination of ductile and brittle behavior.

The HPT-processed samples have fracture surfaces with different features (Fig. 7). Thus, some delamination is observed which is related to the lath martensite in the microstructure (Fig. 7(b)) with a submicron and nano-dimple structure between the delamination (Fig. 7(c, d)). These fine dimples can confirm the ductile fracture behavior of the samples [52, 53]. Also, cave-like shear bands, which are apparent in Fig. 7(d), are produced due to shear deformation. These shear bands grow in length and merge together, thereby having a destructive impact on the measured ductility [54].

5. Summary and conclusions

A combination of intercritical annealing in the dual phase ($\alpha+\gamma$) region at 600 °C for 2 hours and HPT processing was applied to an Fe-10Ni-7Mn (wt. %) martensitic steel for 1 to 20 turns leading to the following results:

1. HPT processing caused the phase transformation of austenite to α'-martensite ($\gamma \rightarrow \alpha'$ and $\gamma \rightarrow \varepsilon \rightarrow \alpha'$). Finally, after 20 turns more than 90% of the microstructure consisted of α'-martensite.
2. Grain size measurements revealed a reduction in the α'-martensite and austenite grain sizes from ~3.8 and ~3.9 μm in the IA sample to ~225 and ~60 nm after 20-turns of HPT,

respectively. The ε-martensite grain size was ~44 nm in the 20-turns HPT sample. Additionally, micro-hardness evolution demonstrated an almost homogenous structure with a maximum value of ~680 Hv after 20 turns.

3. Based on the tensile tests, HPT processing brought improvements in the ultimate and yield strengths together with a decrease in ductility. This conclusion was confirmed by SEM fracture surface images.
4. The equivalent strain applied by HPT on a sample with an initial microstructure consisting of α′-martensite and austenite led to a lower YS and UTS but a higher ductility than in a fully martensitic sample.

Acknowledgments

One of the authors was supported by the European Research Council under ERC Grant Agreement No. 267464-SPDMETALS (TGL).

Data availability

The raw/processed data required to reproduce these findings cannot be shared at this time as the data also forms part of an ongoing study.

References

1. R.Z. Valiev, Y. Estrin, Z. Horita, T.G. Langdon, M.J. Zehetbauer, Y. Zhu, Producing Bulk Ultrafine-Grained Materials by Severe Plastic Deformation: Ten Years Later, JOM 68(4) (2016) 1216-1226. https://doi.org/10.1007/s11837-016-1820-6.
2. K. Edalati, Z. Horita, A review on high-pressure torsion (HPT) from 1935 to 1988, Materials Science and Engineering: A 652 (2016) 325-352. https://doi.org/10.1016/j.msea.2015.11.074.
3. R. Pippan, High-pressure torsion–features and applications, Bulk Nanostructured Materials (2009) 217-232. https://doi.org/10.1002/9783527626892.ch9.
4. A.P. Zhilyaev, T.G. Langdon, Using high-pressure torsion for metal processing: Fundamentals and applications, Progress in Materials Science 53(6) (2008) 893-979. https://doi.org/10.1016/j.pmatsci.2008.03.002.
5. S. Shi, Z. Zhang, X. Wang, G. Zhou, G. Xie, D. Wang, X. Chen, K. Ameyama, Microstructure evolution and enhanced mechanical properties in SUS316LN steel processed by high pressure torsion at room temperature, Materials Science and Engineering: A 711 (2018) 476-483. https://doi.org/10.1016/j.msea.2017.11.064.
6. D.-H. Lee, J.-A. Lee, Y. Zhao, Z. Lu, J.-Y. Suh, J.-Y. Kim, U. Ramamurty, M. Kawasaki, T.G. Langdon, J.-i. Jang, Annealing effect on plastic flow in nanocrystalline CoCrFeMnNi high-entropy alloy: A nanomechanical analysis, Acta Materialia 140 (2017) 443-451. https://doi.org/10.1016/j.actamat.2017.08.057.
7. J. Gubicza, M. El-Tahawy, Y. Huang, H. Choi, H. Choe, J.L. Lábár, T.G. Langdon, Microstructure, phase composition and hardness evolution in 316L stainless steel

processed by high-pressure torsion, Materials Science and Engineering: A 657 (2016) 215-223. https://doi.org/10.1016/j.msea.2016.01.057.

8. X.H. An, Q.Y. Lin, G. Sha, M.X. Huang, S.P. Ringer, Y.T. Zhu, X.Z. Liao, Microstructural evolution and phase transformation in twinning-induced plasticity steel induced by high-pressure torsion, Acta Materialia 109 (2016) 300-313. https://doi.org/10.1016/j.actamat.2016.02.045.
9. J. Čížek, M. Janeček, T. Vlasák, B. Smola, O. Melikhova, D. SV, The development of vacancies during severe plastic deformation, Materials transactions 60(8) (2019) 1533-1542. https://doi.org/10.2320/matertrans.MF201937.
10. T. Müller, M.W. Kapp, A. Bachmaier, P. Felfer, R. Pippan, Ultrahigh-strength low carbon steel obtained from the martensitic state via high pressure torsion, Acta Materialia 166 (2019) 168-177. https://doi.org/10.1016/j.actamat.2018.12.028.
11. T. Müller, A. Bachmaier, A. Stark, N. Schell, R. Pippan, Nanostructured Low Carbon Steels Obtained from the Martensitic State via Severe Plastic Deformation, Precipitation, Recovery, and Recrystallization, Advanced Engineering Materials 21(1) (2019) 1800202. https://doi.org/10.1002/adem.201800202.
12. M. El-Tahawy, Y. Huang, H. Choi, H. Choe, J.L. Lábár, T.G. Langdon, J. Gubicza, High temperature thermal stability of nanocrystalline 316L stainless steel processed by high-pressure torsion, Materials Science and Engineering: A 682 (2017) 323-331. https://doi.org/10.1016/j.msea.2016.11.066.
13. C. Xu, S.V. Dobatkin, Z. Horita, T.G. Langdon, Superplastic flow in a nanostructured aluminum alloy produced using high-pressure torsion, Materials Science and Engineering: A 500(1-2) (2009) 170-175. https://doi.org/10.1016/j.msea.2008.09.049.

14. P.H.R. Pereira, Y. Huang, M. Kawasaki, T.G. Langdon, An examination of the superplastic characteristics of Al–Mg–Sc alloys after processing, Journal of Materials Research 32(24) (2017) 4541-4553. https://doi.org/10.1557/jmr.2017.286.
15. H. Shahmir, M. Nili-Ahmadabadi, Y. Huang, J. Myun Jung, H. Seop Kim, T.G. Langdon, Shape memory effect in nanocrystalline NiTi alloy processed by high-pressure torsion, Materials Science and Engineering: A 626 (2015) 203-206. https://doi.org/10.1016/j.msea.2014.12.056.
16. Y. Mine, K. Tachibana, Z. Horita, Effect of High-Pressure Torsion Processing and Annealing on Hydrogen Embrittlement of Type 304 Metastable Austenitic Stainless Steel, Metallurgical and Materials Transactions A 41(12) (2010) 3110-3120. https://doi.org/10.1007/s11661-010-0394-0.
17. N. Adachi, N. Wu, Y. Todaka, H. Sato, R. Ueji, Phase transformation in Fe–Mn–C alloys by severe plastic deformation under high pressure, Materials Letters 185 (2016) 109-111. https://doi.org/10.1016/j.matlet.2016.08.113.
18. K. Yan, D. Bhattacharyya, Q. Lian, S. Kabra, M. Kawasaki, D.G. Carr, M.D. Callaghan, M. Avdeev, H. Li, Y. Wang, X. Liao, T.G. Langdon, K.-D. Liss, R.J. Dippenaar, Martensitic Phase Transformation and Deformation Behavior of Fe-Mn-C-Al Twinning-Induced Plasticity Steel during High-Pressure Torsion, Advanced Engineering Materials 16(7) (2014) 927-932. https://doi.org/10.1002/adem.201300488.
19. Y. Sun, M. Aindow, R. Hebert, T.G. Langdon, E. Lavernia, High-pressure torsion-induced phase transformations and grain refinement in Al/Ti composites, Journal of Materials Science 52(20) (2017) 12170-12184. https://doi.org/10.1007/s10853-017-1331-z.

20. A. Bachmaier, R. Pippan, High-Pressure Torsion Deformation Induced Phase Transformations and Formations: New Material Combinations and Advanced Properties, Materials transactions 60(7) (2019) 1256-1269. https://doi.org/10.2320/matertrans.MF201930.
21. J.-K. Han, K.-D. Liss, T.G. Langdon, M. Kawasaki, Synthesis of a bulk nanostructured metastable Al alloy with extreme supersaturation of Mg, Scientific Reports 9(1) (2019) 1-7. https://doi.org/10.1038/s41598-019-53614-3.
22. T. Mousavi, J. Dai, P. Bazarnik, P.H.R. Pereira, Y. Huang, M. Lewandowska, T.G. Langdon, Fabrication and characterization of nanostructured immiscible Cu–Ta alloys processed by high-pressure torsion, Journal of Alloys and Compounds (2020) 155007. https://doi.org/10.1016/j.jallcom.2020.155007.
23. R.Z. Valiev, T.G. Langdon, Principles of equal-channel angular pressing as a processing tool for grain refinement, Progress in Materials Science 51(7) (2006) 881-981. https://doi.org/10.1016/j.pmatsci.2006.02.003.
24. J. Wongsa-Ngam, M. Kawasaki, T.G. Langdon, A comparison of microstructures and mechanical properties in a Cu–Zr alloy processed using different SPD techniques, Journal of Materials Science 48(13) (2013) 4653-4660. https://doi.org/10.1007/s10853-012-7072-0.
25. S.H. Nedjad, M.N. Ahmadabadi, T. Furuhara, Transmission electron microscopy study on the grain boundary precipitation of an Fe-Ni-Mn maraging steel, Metallurgical and Materials Transactions A 39(1) (2008) 19-27. https://doi.org/10.1007/s11661-007-9407-z.

26. H. Shirazi, M. Nili-Ahmadabadi, A. Fatehi, S. Hossein Nedjad, Effect of Severe Plastic Deformation on Mechanical Properties of Fe-Ni-Mn High Strength Steel, Advanced Materials Research 83-86 (2009) 16-23. https://doi.org/10.4028/www.scientific.net/AMR.83-86.16.

27. H. Koohdar, M. Nili-Ahmadabadi, M. Habibi-Parsa, H. Ghasemi-Nanesa, Investigating on the Reverse Transformation of Martensite to Austenite and Pseudoelastic Behavior in Ultrafine-Grained Fe-10Ni-7Mn (wt %) Steel Processed by Heavy Cold Rolling, Advanced Materials Research 829 (2013) 25-29. https://doi.org/10.4028/www.scientific.net/AMR.829.25.

28. H. Ghasemi-Nanesa, M. Nili-Ahmadabadi, H.R. Koohdar, M. Habibi-Parsa, S. Hossein Nedjad, S.A. Alidokht, T.G. Langdon, Strain-induced martensite to austenite reverse transformation in an ultrafine-grained Fe–Ni–Mn martensitic steel, Philosophical Magazine 94(13) (2014) 1493-1507. https://doi.org/10.1080/14786435.2014.886785.

29. H.R. Koohdar, M. Nili-Ahmadabadi, M. Habibi-Parsa, H.R. Jafarian, H. Ghasemi-Nanesa, H. Shirazi, Observation of pseudoelasticity in a cold rolled Fe–Ni–Mn martensitic steel, Materials Science and Engineering: A 658 (2016) 86-90. https://doi.org/10.1016/j.msea.2016.01.113.

30. A. Mirsepasi, M. Nili-Ahmadabadi, M. Habibi-Parsa, H. Ghasemi-Nanesa, A.F. Dizaji, Microstructure and mechanical behavior of martensitic steel severely deformed by the novel technique of repetitive corrugation and straightening by rolling, Materials Science and Engineering: A 551 (2012) 32-39. https://doi.org/10.1016/j.msea.2012.04.073.

31. F. Javadzadeh Kalahroudi, H. Koohdar, H.R. Jafarian, Y. Huang, T.G. Langdon, M. Nili-Ahmadabadi, On the microstructure and mechanical properties of an Fe-10Ni-7Mn

martensitic steel processed by high-pressure torsion, Materials Science and Engineering: A 749 (2019) 27-34. https://doi.org/10.1016/j.msea.2019.02.002.

32. H. Koohdar, M. Nili-Ahmadabadi, M. Habibi-Parsa, H.R. Jafarian, T. Bhattacharjee, N. Tsuji, On the Stability of Reversely Formed Austenite and Related Mechanism of Transformation in an Fe-Ni-Mn Martensitic Steel Aided by Electron Backscattering Diffraction and Atom Probe Tomography, Metallurgical and Materials Transactions A 48(11) (2017) 5244-5257. https://doi.org/10.1007/s11661-017-4288-2.
33. H.R. Koohdar, M. Nili-Ahmadabadi, M. Habibi-Parsa, H.R. Jafarian, Development of pseudoelasticity in Fe–10Ni–7Mn (wt%) high strength martensitic steel by intercritical heat treatment and subsequent ageing, Materials Science and Engineering: A 621 (2015) 52-60. https://doi.org/10.1016/j.msea.2014.10.049.
34. R.B. Figueiredo, P.H.R. Pereira, M.T.P. Aguilar, P.R. Cetlin, T.G. Langdon, Using finite element modeling to examine the temperature distribution in quasi-constrained high-pressure torsion, Acta Materialia 60(6-7) (2012) 3190-3198. https://doi.org/10.1016/j.actamat.2012.02.027.
35. H. Shirazi, G. Miyamoto, S. Hossein Nedjad, H. Ghasemi-Nanesa, M. Nili Ahmadabadi, T. Furuhara, Microstructural evaluation of austenite reversion during intercritical annealing of Fe–Ni–Mn martensitic steel, Journal of Alloys and Compounds 577 (2013) S572-S577. https://doi.org/10.1016/j.jallcom.2012.02.015.
36. M. El-Tahawy, J. Gubicza, Y. Huang, H.L. Choi, H.M. Choe, J.L. Lábár, T.G. Langdon, Evolution of Microstructure, Phase Composition and Hardness in 316L Stainless Steel Processed by High-Pressure Torsion, Materials Science Forum 879 (2016) 502-507. https://doi.org/10.4028/www.scientific.net/MSF.879.502.

37. A.K. De, J.G. Speer, D.K. Matlock, D.C. Murdock, M.C. Mataya, R.J. Comstock, Deformation-induced phase transformation and strain hardening in type 304 austenitic stainless steel, Metallurgical and Materials Transactions A 37(6) (2006) 1875-1886. https://doi.org/10.1007/s11661-006-0130-y.

38. H. Ghasemi-Nanesa, M. Nili-Ahmadabadi, H. Shirazi, S. Hossein Nedjad, S.H. Pishbin, Ductility enhancement in ultrafine-grained Fe–Ni–Mn martensitic steel by stress-induced reverse transformation, Materials Science and Engineering: A 527(29-30) (2010) 7552-7556. https://doi.org/10.1016/j.msea.2010.08.028.

39. C.X. Huang, G. Yang, Y.L. Gao, S.D. Wu, S.X. Li, Investigation on the nucleation mechanism of deformation-induced martensite in an austenitic stainless steel under severe plastic deformation, Journal of Materials Research 22(3) (2011) 724-729. https://doi.org/10.1557/jmr.2007.0094.

40. L. Murr, K. Staudhammer, S. Hecker, Effects of strain state and strain rate on deformation-induced transformation in 304 stainless steel: Part II. Microstructural study, Metallurgical Transactions A 13(4) (1982) 627-635. https://doi.org/10.1007/BF02644428.

41. Y. Cao, S. Ni, X. Liao, M. Song, Y. Zhu, Structural evolutions of metallic materials processed by severe plastic deformation, Materials Science and Engineering: R: Reports 133 (2018) 1-59. https://doi.org/10.1016/j.mser.2018.06.001.

42. Y.Z. Tian, J.J. Li, P. Zhang, S.D. Wu, Z.F. Zhang, M. Kawasaki, T.G. Langdon, Microstructures, strengthening mechanisms and fracture behavior of Cu–Ag alloys processed by high-pressure torsion, Acta Materialia 60(1) (2012) 269-281. https://doi.org/10.1016/j.actamat.2011.09.058.

43. D.M. Marulanda Cardona, J. Wongsa-Ngam, T.G. Langdon, Microstructural evolution and microhardness in a low carbon steel processed by high-pressure torsion, Journal of Materials Research and Technology 3(4) (2014) 344-348. https://doi.org/10.1016/j.jmrt.2014.09.004.

44. M. Kawasaki, R.B. Figueiredo, T.G. Langdon, An investigation of hardness homogeneity throughout disks processed by high-pressure torsion, Acta Materialia 59(1) (2011) 308-316. https://doi.org/10.1016/j.actamat.2010.09.034.

45. S. Mohd Yusuf, Y. Chen, S. Yang, N. Gao, Microstructural evolution and strengthening of selective laser melted 316L stainless steel processed by high-pressure torsion, Materials Characterization 159 (2020) 110012. https://doi.org/10.1016/j.matchar.2019.110012.

46. Y. Estrin, A. Molotnikov, C. Davies, R. Lapovok, Strain gradient plasticity modelling of high-pressure torsion, Journal of the Mechanics and Physics of Solids 56(4) (2008) 1186-1202. https://doi.org/10.1016/j.jmps.2007.10.004.

47. Y. Huang, M. Kawasaki, T.G. Langdon, An investigation of flow patterns and hardness distributions using different anvil alignments in high-pressure torsion, Journal of Materials Science 48(13) (2013) 4533-4542. https://doi.org/10.1007/s10853-012-7015-9.

48. Y. Huang, M. Kawasaki, T.G. Langdon, An evaluation of the shearing patterns introduced by different anvil alignments in high-pressure torsion, Journal of Materials Science 49(8) (2014) 3146-3157. https://doi.org/10.1007/s10853-014-8015-8.

49. W. Jiang, H. Zhou, Y. Cao, J. Nie, Y. Li, Y. Zhao, M. Kawasaki, T.G. Langdon, Y. Zhu, On the Heterogeneity of Local Shear Strain Induced by High□Pressure Torsion,

Advanced Engineering Materials 22(1) (2019) 1900477. https://doi.org/10.1002/adem.201900477.

50. Y. Huang, M. Kawasaki, T.G. Langdon, Influence of Anvil Alignment on Shearing Patterns in High□Pressure Torsion, Advanced Engineering Materials 15(8) (2013) 747-755. https://doi.org/10.1002/adem.201200363.
51. K. Edalati, T. Fujioka, Z. Horita, Evolution of Mechanical Properties and Microstructures with Equivalent Strain in Pure Fe Processed by High Pressure Torsion, Materials Transactions 50(1) (2009) 44-50. https://doi.org/10.2320/matertrans.MD200812.
52. M.V. Karavaeva, S.K. Kiseleva, M.M. Abramova, A.V. Ganeev, R.Z. Valiev, Microstructure, properties, and failure characteristics of medium-carbon steel subjected to severe plastic deformation, IOP Conference Series: Materials Science and Engineering 63 (2014) 012056. https://doi.org/10.1088/1757-899x/63/1/012056.
53. A. Hohenwarter, A. Taylor, R. Stock, R. Pippan, Effect of Large Shear Deformations on the Fracture Behavior of a Fully Pearlitic Steel, Metallurgical and Materials Transactions A 42(6) (2010) 1609-1618. https://doi.org/10.1007/s11661-010-0541-7.
54. C. Ruffing, A. Kobler, E. Courtois-Manara, R. Prang, C. Kübel, Y. Ivanisenko, E. Kerscher, Fatigue Behavior of Ultrafine-Grained Medium Carbon Steel with Different Carbide Morphologies Processed by High Pressure Torsion, Metals 5(2) (2015) 891-909. https://doi.org/10.3390/met5020891.

Table captions

Table 1. Chemical composition of the investigated steel.

Table 2. Average grain sizes of the different phases obtained from EBSD images

Table 3. Values of ultimate tensile strength, yield strength and fracture strain for the samples.

Figure Captions

Fig. 1. Dimensions of disk samples including positions for microstructure observation, micro-hardness measurements and tensile test sample.

Fig. 2. EBSD phase maps for (a) SA sample including high density of low-angle grain boundaries, (b) IA sample at 600 °C including austenite- martensite network, and HPT-processed samples after (c) 1 turn with fewer low-angle grain boundaries than SA sample but elongated ε-martensite and fine austenite, (d) 6 turns with fine ε-martensite, (e) 20 turns including mainly α′-martensite with very fine and few ε-martensite and austenite.

Fig. 3. EBSD results of volume fractions of α′-martensite, austenite and ε-martensite phases in SA, IA at 600 ˚C and HPT-processed samples for 1, 6 and 20 turns.

Fig. 4. (a) Micro-hardness distribution recorded across the diameter of the IA and HPT-processed samples, and (b) Micro-hardness values against equivalent strain after HPT processing for different numbers of turns.

Fig. 5. Engineering stress-strain curves of the samples. HPT- processed sample after 3 turns depicts optimum UTS and ductility.

Fig. 6. SEM images of fracture surfaces of the (a, b) SA sample, and (c, d) IA sample.

Fig. 7. SEM images of fracture surfaces of the HPT- processed sample after 20 turns with ductile- brittle mode.

Table 1. Chemical composition of the investigated steel.

Element	Fe	Ni	Mn	C	S	P	N	Al
wt. %	Bal.	10.05	6.97	0.005	0.006	0.005	0.005	0.003

Table 2. Average grain sizes of the different phases obtained from EBSD images.

	α′-martensite	austenite	ε-martensite
SA	□ 5.5 μm	-	-
IA at 600°C	□ 3.8 μm	□ 3.9 μm	-
IA at 600°C + HPT (N=1)	□ 546 nm	□ 385 nm	□ 435 nm
IA at 600°C + HPT (N=6)	□ 524 nm	□ 107 nm	□ 221 nm
IA at 600°C + HPT (N=20)	□ 223 nm	□ 62 nm	□ 44 nm

Table 3. Values of ultimate tensile strength, yield strength and fracture strain for the samples.

	UTS (MPa)	YS (MPa)	Fracture Strain (%)	Ref.
SA	830	790	16.5	[31]
IA at 600°C	795	510	27.8	Present
IA at 600°C+ HPT (N=3)	1055	1040	20.3	Present
IA at 600°C+ HPT (N=10)	1600	1440	7.3	Present
IA at 600°C+ HPT (N=20)	2235	2150	2.4	Present
SA+ HPT (N=3)	1840	1800	10.2	[31]
SA+ HPT (N=10)	2115	1995	6.4	[31]
SA+ HPT (N=20)	2230	2040	3.1	[31]

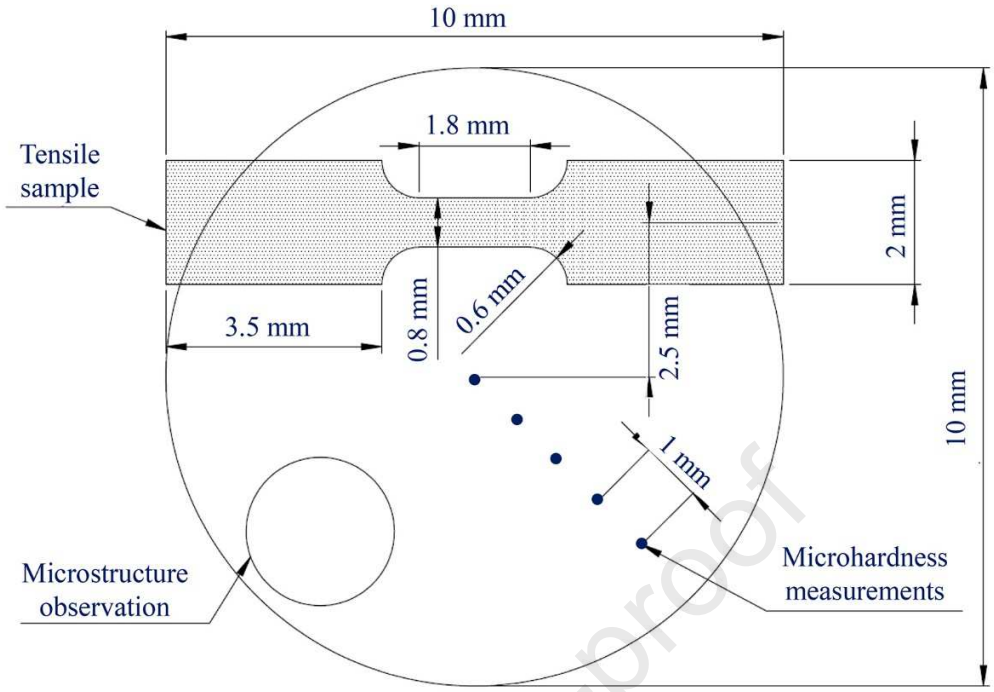

Fig. 1. Dimensions of disk samples including positions for microstructure observation, micro-hardness measurements and tensile test sample.

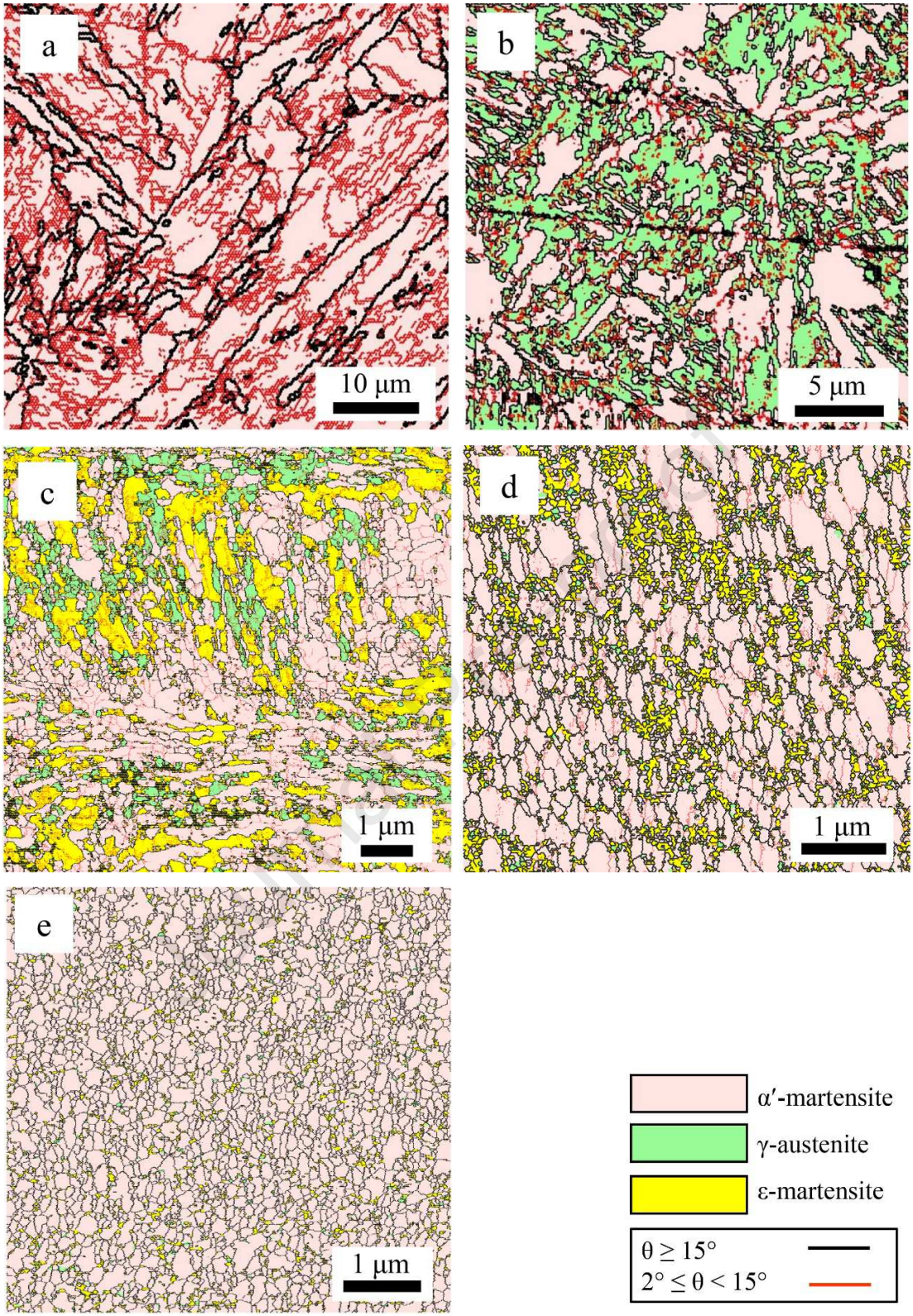
a
10 μm
b
5 μm
c
1 μm
d
1 μm
e
1 μm
α′-martensite
γ-austenite
ε-martensite
θ ≥ 15°
2° ≤ θ < 15°

Fig. 2. EBSD phase maps for (a) SA sample including high density of low-angle grain boundaries, (b) IA sample at 600 ˚C including austenite- martensite network, and HPT-processed samples after (c) 1 turn with fewer low-angle grain boundaries than SA sample but elongated ε-martensite and fine austenite, (d) 6 turns with fine ε-martensite, (e) 20 turns including mainly α′-martensite with very fine and few ε-martensite and austenite.

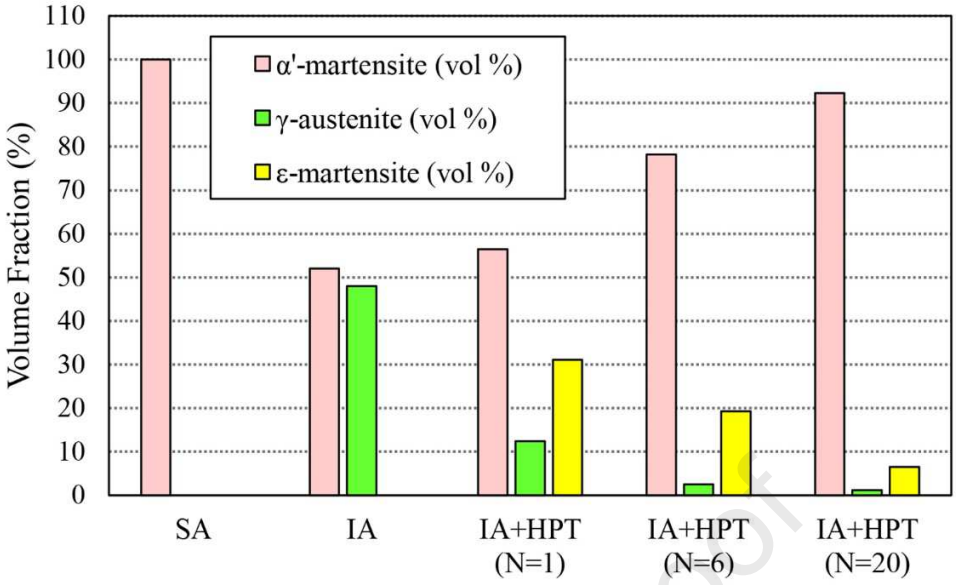

Fig. 3. EBSD results of volume fractions of α′-martensite, austenite and ε-martensite phases in SA, IA at 600 ˚C and HPT-processed samples for 1, 6 and 20 turns.

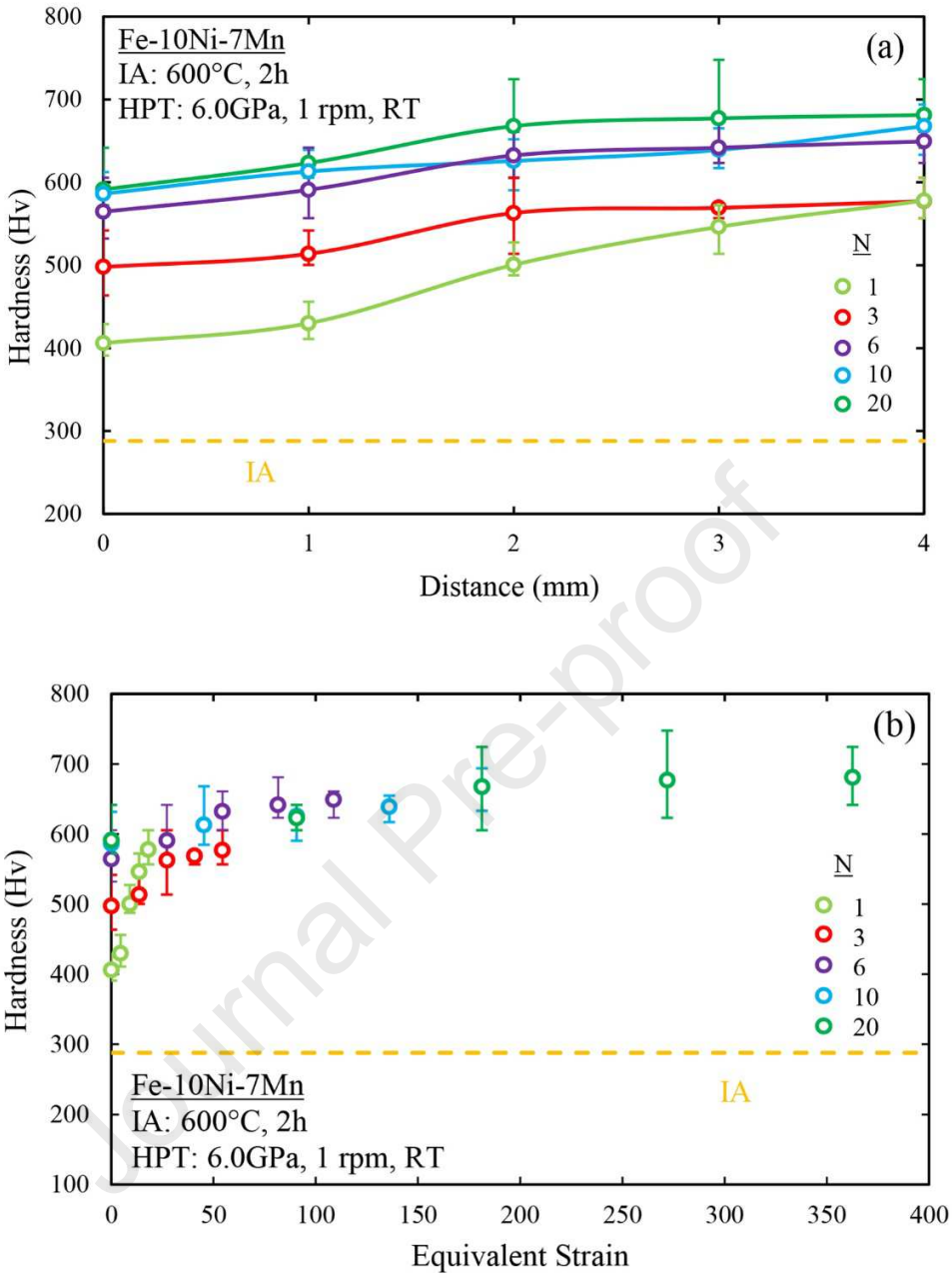

Fig. 4. (a) Micro-hardness distribution recorded across the diameter of the IA and HPT-processed samples, and (b) Micro-hardness values against equivalent strain after HPT processing for different numbers of turns.

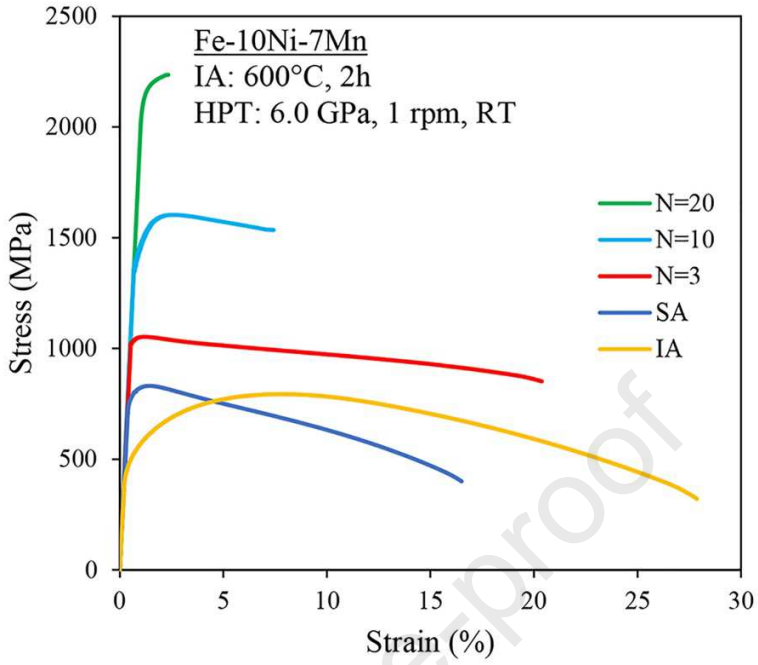

Fig. 5. Engineering stress-strain curves of the samples. HPT- processed sample after 3 turns depicts optimum UTS and ductility.

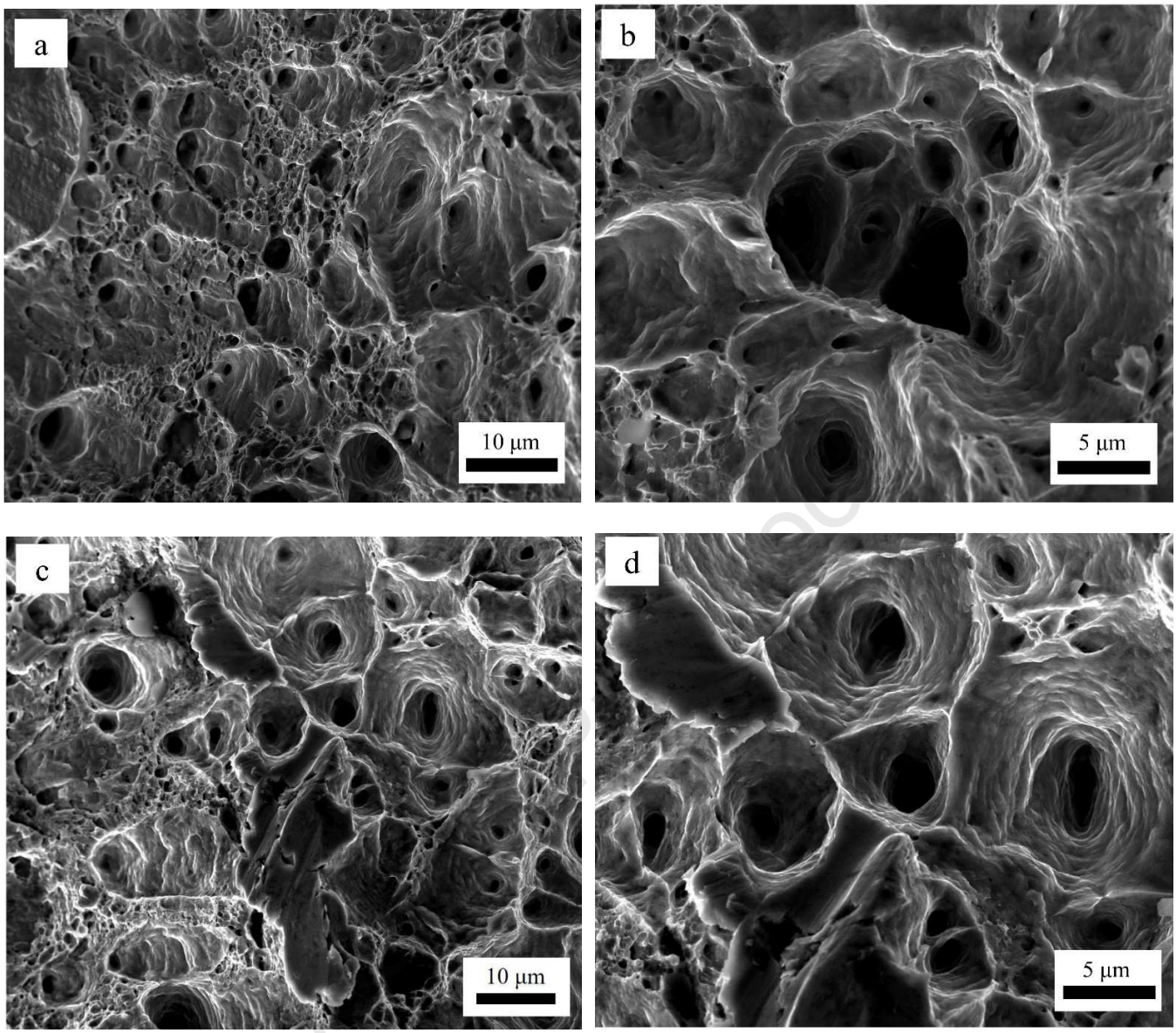

Fig. 6. SEM images of fracture surfaces of the (a, b) SA sample, and (c, d) IA sample.

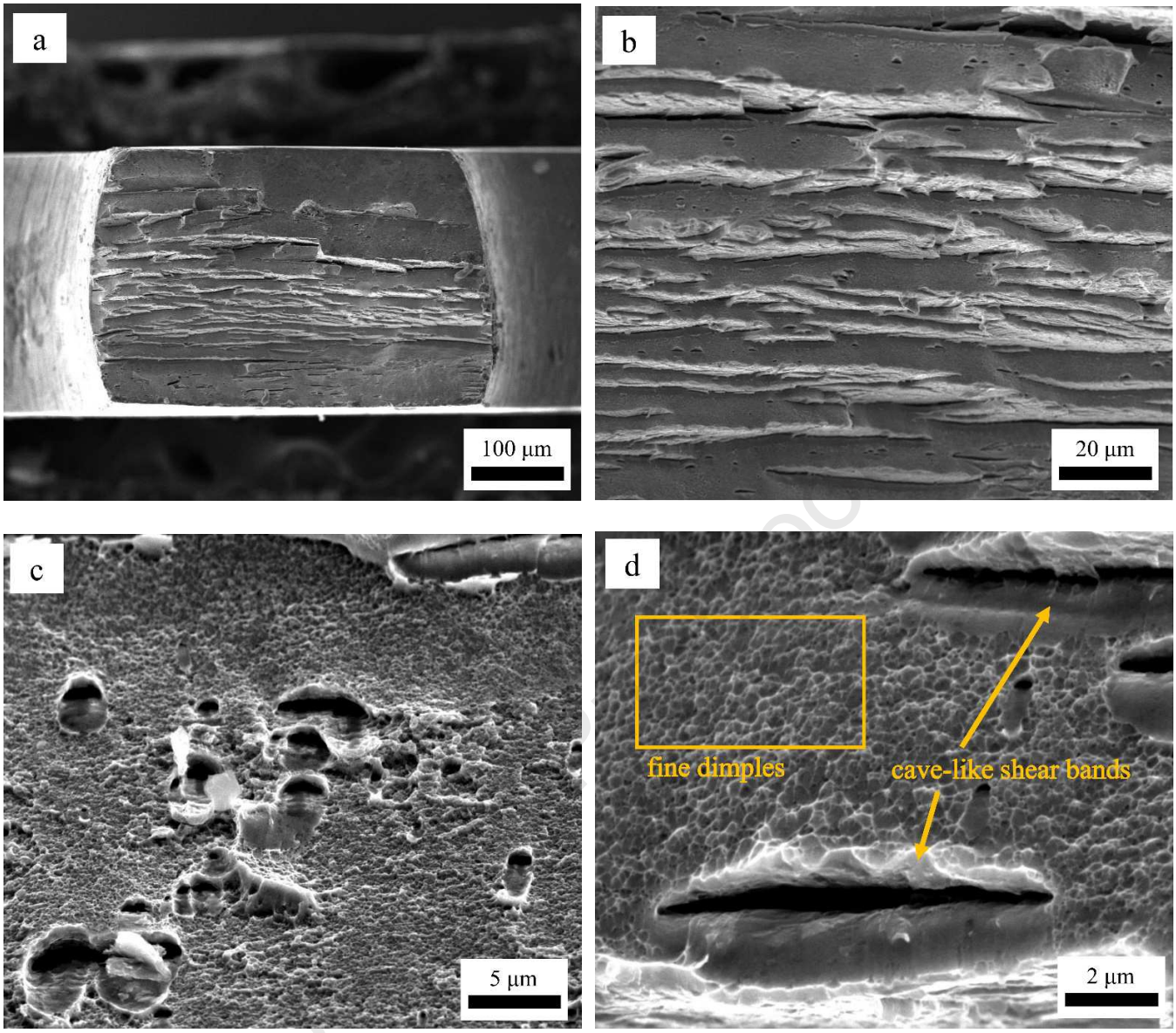

Fig. 7. SEM images of fracture surfaces of the HPT- processed sample after 20 turns with ductile- brittle mode.

Declaration of interests

☒ The authors declare that they have no known competing financial interests or personal relationships that could have appeared to influence the work reported in this paper.

☐The authors declare the following financial interests/personal relationships which may be considered as potential competing interests: